DISTURBANCE FUNCTIONS OF THE GÖRTLER INSTABILITY ON AN AIRFOIL

ICAS-86-1.8.1

J. Ray Dagenhart
Aerospace Engineer
Transonic Aerodynamics Division
NASA Langley Research Center
Hampton, Virginia 23665-5225

S. M. Mangalam
Senior Scientist
Analytical Services and Materials, Inc.
Hampton, Virginia 23666

Abstract

Görtler vortices arise in boundary layers along concave surfaces due to centrifugal effects. This paper presents some results of an experiment conducted to study the development of these vortices on an airfoil with a pressure gradient in the concave region where an attached laminar boundary layer was insured with suction through a perforated panel. A sublimating chemical technique was used to visualize Görtler vortices and the velocity field was measured by laser velocimetry. The vortex wavelength clearly varied with Görtler number as predicted by linear theory. Experimental disturbance functions are compared with those predicted by the linear stability theory. The trend of vortex amplification in the concave zone and damping in the following convex region is shown to essentially follow the theoretical predictions.

Nomenclature

C_p	pressure coefficient
c	chord length
$G = \frac{U_e \delta_D}{\nu}\sqrt{\frac{\delta_D}{r}}$	Görtler number
G_M	Görtler number evaluated at maximum curvature
M_∞	free-stream Mach number
R_c	Reynolds number based on chord
r	radius of curvature
U_e	boundary-layer edge velocity
U_∞	free-stream velocity
U,V,W	velocity components in laser coordinates
u,v,w	velocity components in the body-centered coordinate system
u_{rms}	root mean square over the span of the streamwise disturbance velocity component
x,y,z	model coordinates
$\alpha\delta_D = \frac{2\pi\delta_D}{\lambda}$	nondimensional wave number
β	Görtler vortex growth rate
$\delta_D = \delta^*/1.7208$	boundary layer thickness parameter
$\delta_r = \sqrt{\frac{\nu x}{U_\infty}}$	Blasius boundary-layer thickness parameter
δ^*	boundary-layer displacement thickness
$\eta = y/\delta_D$	nondimensional normal coordinate
$\Lambda = \frac{U_e r}{\nu}\left(\frac{\lambda}{r}\right)^{3/2}$	nondimensional wavelength
λ	wavelength
ν	kinematic viscosity

Introduction

Görtler vortices arise in boundary layers along concave surfaces due to centrifugal effects. These counter-rotating streamwise vortices are one of three known flow instabilities which lead to boundary-layer transition. Coupled with Tollmien-Schlichting waves and crossflow vortices, the Görtler vortices can trigger early transition to turbulence. Görtler vortices may play an important role in internal flows with concave curvature and on modern supercritical laminar-flow-control wings which have concave regions near the leading and trailing edges of the lower surface.

Centrifugal instability in concentric rotating cylinders was first examined by Taylor.[1] The centrifugal instability of boundary-layer flows over concave walls was first treated analytically by Görtler[2] after whom the vortices are named. The stability is governed by the parameter

$$G = \frac{U_e \delta_D}{\nu}\sqrt{\frac{\delta_D}{r}}$$

where δ_D is a suitable boundary layer thickness, r is the radius of curvature, and ν is the fluid kinematic viscosity. Many studies have since been devoted to the improvement and extension of Görtler's analysis and a thorough survey of these efforts has been reported by Herbert.[3] The influences of streamline curvature and far-field boundary conditions were analyzed by Floryan and Saric.[4] Pressure gradient effects were considered by Ragab and Nayfeh.[5] Hall integrated the partial differential equations for the Görtler instability in a growing boundary layer.[6]

There have also been a number of experimental studies of this problem, mostly conducted in curved channel flows. Tani and Aihara[7] attempted to correlate the streamwise vortex wavelength with wall curvature and free-stream velocity (i.e., Görtler number) as predicted by

theory. The failure to find such a correlation led them to the conclusion that the vortex wavelength is determined more by the particular edge effects of the experimental apparatus and less by the curvature of the model or the velocity of the oncoming flow. Several other experimenters, including Bippes, have also found that the wavelength is essentially independent of the Görtler number.[8] Bippes did find that when the stream turbulence was made isotropic, the most amplified disturbances, according to theory, could be generated.[8] Experimental data from these studies seem to indicate that some preferred wave number disturbance is selected initially from those unstable ones and is amplified with increasing Görtler number while maintaining a constant wavelength.

In the present experiment, a sublimating chemical technique was used to visualize the Görtler vortices and the velocity field was measured using laser velocimetry. The vortex wavelength was determined from both the flow visualization and measured velocity data. The experimentally determined disturbance functions are compared to theoretical predictions obtained using Floryan's code.[9] Some results of this experiment have been previously reported by Mangalam, Dagenhart, Hepner, and Meyers[10] and by Dagenhart and Mangalam.[11]

Test Apparatus

The 1.83m chord airfoil model was tested in the NASA Langley Low-Turbulence Pressure Tunnel (LTPT). A photograph of the model is shown in figure 1. The model consists of two parts - a structural element and a test element. The test element includes the leading edge and the upper surface back to midchord. The structural element consists of the spar and the remainder of the airfoil surface including a 10 percent chord flap. With this design, several test region geometries can be examined. The present test element includes a concave region from x/c = 0.175 to x/c = 0.275. The minimum radius of curvature is 0.24m. Attached laminar boundary-layer flow is insured by means of suction through a 0.11 x 0.76m perforated titanium panel located in the compression part of the concave region. The suction region is divided into three spanwise suction strips. The suction in each strip is independently controlled by its own needle valve. The model surface is painted flat black over gel coat and fiberglass. Figure 2 shows the model pressure distribution. The 10 percent chord flap was used to control the stagnation point location and to maintain a flat or slightly favorable pressure gradient ahead of the concave region.

The LTPT is a pressurized, closed-circuit, continuous flow wind tunnel. The test section is 2.29m high, 2.29m long, and 0.91m wide. The contraction ratio is 17.6. The tunnel has excellent flow quality due, in part, to the nine screens in the settling chamber. The velocity fluctuations in the test section were found to be 0.025 percent at 0.05 Mach number.[12] The pressure fluctuations at the test section wall, normalized with respect to free-stream pressure, were approximately 10^{-5} at this Mach number.[12]

The present experiment was conducted at atmospheric pressure. The chord Reynolds number was varied from 1.0 million to 5.9 million and the Mach number ranged from 0.024 to 0.125 yielding Görtler numbers of up to 16.

A specialized, single axis, three-component laser velocimeter was used to study the flow field in the test region. The single axis, five-beam optical configuration uses the standard two color, two-component beam pattern with the two green beams (514.5nm) arranged in the horizontal plane and the two blue beams (488.0nm) arranged in the vertical plane forming a diamond pattern to measure the U or streamwise component (green beams) and the V or vertical component (blue beams). A third green beam is placed along the optical axis bisecting the angle between the original two green beams. This arrangement allows for the measurement of the three orthogonal velocity components: U, V, and W. The flow was seeded with tridecane particles using a particle generator located upstream of the settling chamber screens. The LV data were recorded and processed by a dedicated computer system. The velocity components were measured in the laser velocimeter coordinate system which looked down on the model at an angle of 11°. These velocity components were then transformed into wind tunnel and model coordinate systems for analysis.

Results and Discussion

A thin layer of solid white biphenyl material was sprayed over the black model surface to visualize the flow. This hydrocarbon material sublimes due to the heat transfer at the airfoil surface which is proportional to the surface shear stress.[13] The flow pattern is made visible due to the differential surface shear stress distribution under the layer of counter-rotating Görtler vortices. Elapsed times of about 30 minutes to 1 hour were required for the pattern to emerge clearly, depending on the free-stream velocity. Representative flow patterns are shown in Figures 3(a), (b), and (c) taken at chord Reynolds numbers of 2.24, 3.21, and 3.67 million, respectively. The dark bands represent the high shear stress regions where the chemical layer has sublimed revealing the black background of the airfoil surface, whereas, the white bands correspond to low shear regions. A set of black and white bands constitutes a pair of counter-rotating vortices and represents the wavelength of these vortices.

The photographs in figure 3 show the region $0.20 < x/c < 0.40$ near the center of the model span. The perforated titanium suction panel is visible at the upstream edge of each photograph. No streamwise streaks were observed in the region ahead of the concave zone. The streaks observed downstream of the suction panel are essentially uniformly spaced along the span. Wavelength was determined by taking the average of the number of pairs of streaks over a 15cm to 45cm span. The nondimensional wavelength parameter Λ was computed using this value of dimensional wavelength and the mean flow and geometric parameters. The dimensional wavelength appears to remain constant throughout the concave region. Beyond the concave region, the streaks decrease considerably in

contrast but remain visible back to the jagged transition line. This indicates damping of the Görtler vortices in the convex region, which is confirmed by the laser velocimeter measurements discussed below. Furthermore, in the convex zone, occasional vortex mergers are visible.

Velocity measurements were made at chord locations of x/c = 0.175, 0.20, 0.225, 0.25, 0.275, 0.30, and 0.3375. Figure 4 shows the variation of the streamwise velocity component along the span from 1.5cm to 4.5cm left of midspan at several heights above the model surface[10]. These are at a location of x/c = 0.25 and chord Reynolds number of $R_c = 1.0 \times 10^6$. The spanwise periodicity of the streamwise velocity component is evident in figure 4. The wavelength of this variation is approximately $\lambda = 0.8$cm. This wavelength is slightly larger than that previously reported in reference 10 where the data were not accurately filtered. The maximum disturbance amplitude occurs at approximately y = 0.09cm. Data for the other chord locations similar to those of figure 4 are given in reference 10.

Figures 5-9 show the streamwise disturbance velocity variation along the span, the power spectral density, and the autocorrelation function for each height above the model surface at x/c = 0.25 and $R_c = 1.0 \times 10^6$. All three velocity components (U, V, and W) were measured in the laser coordinate system. These were transformed successively to the tunnel coordinate system and then to the model coordinate system. In all three coordinate systems, the velocity component essentially along the span is quite small. In the laser and tunnel coordinate systems both the U and V velocity components are finite in magnitude and exhibit periodic variations along the span. However, when the velocity is transformed into model-centered coordinates with components u, v, w being streamwise, normal, and spanwise, only the streamwise component has a finite value significantly larger than the measurement uncertainty. Therefore, only the streamwise velocity data are presented here.

The velocity data were measured by scanning the laser control volume spanwise from z = 1.5cm to 4.5cm in steps of 0.05cm at a constant nominal height above the model surface. The control volume was then moved normal to the surface to the next measurement height and scanned back to z = 1.5. This process normally took approximately five hours per chord location. Some of the velocity data presented in reference 10 show a general decrease in velocity with increasing z. This is caused by minute deflections of the floor supporting the heavy laser optics traversing mechanism. This error has been partially corrected in the disturbance velocities of figures 5a-9a by considering the mean velocity to be a linear function of z. The data are shown as $(u - u_1)/U_e$ for each height where u_1 is the least squares linear fit of the data and U_e is the local boundary-layer edge velocity. The streamwise velocity disturbances at each height can be seen to vary by up to $\pm$ 5% of the local edge velocity in figures 5a-9a. The maximum amplitude seems to occur at y = 0.09cm. For heights of y = 0.04, 0.06, 0.09, and 0.13cm above the model surface, figures 6a-9a clearly show that the velocity disturbances are periodic with wavelength $\lambda \approx 0.8$cm. At y = 0.18 cm, the periodicity is less obvious probably because the disturbance amplitude is smaller there.

The power spectral density functions corresponding to the streamwise velocity variations for several heights are shown as functions of wavelength in figures 5b-9b. In each figure, the dominant wavelength clearly occurs in the range $0.64 < \lambda < 0.96$cm with the maximum near $\lambda = 0.8$cm. This is in accord with the earlier direct observations of the periodicity of the velocity variations. Even at y = 0.18 cm (fig. 5b), this dominant wavelength is obvious in the power spectral density although it was not so apparent in the velocity data (fig. 5a). At several measurement heights, the power spectral density shows considerable content at large wavelengths $\lambda > 1.5$cm. These are not considered to be significant since the spanwise measurement range covered only 3 cm. The autocorrelation functions shown in figure 5c-9c also clearly show the periodicity at all measurement heights with wavelength $\lambda \approx 0.8$cm. This is in agreement with both the velocity data and the power spectral density functions. The periodicity is evident in peak-to-peak, valley-to-valley, and in most cases, the zero-crossing wavelength.

Results similar to those of figures 5-9 were obtained for the other measurement locations, but are not shown here. Laser velocimeter measurements of streamwise velocity at all chord locations as well as at all heights above the surface were used to determine disturbance wavelength using statistical methods. Except where a secondary instability was present, the wavelength did not vary by more than 10 percent throughout the measurement zone at a given free stream condition. Wavelengths, determined from laser measurements, agree well with those observed in flow visualization. As in all previous experiments, the dimensional wavelength of the disturbance was conserved in the flow direction, but unlike earlier experments, the wavelength was observed to vary appreciably with free stream conditions. The variation in wavelength was most noticeable at lower speeds as seen from figure 10 where λ is plotted against Görtler number. The theoretical curve corresponds to the wavelength computed from maximum amplification conditions.[9] It is seen that experimental values of λ lie very close to wavelengths predicted on the basis of linear theory. The nondimensional wavelength parameter Λ obtained from flow visualization and laser velocimeter measurements is also shown plotted as a function of Görtler number in figure 11 where it is compared with existing experimental data due to Tani and Sakagami[14] and Bippes[8] and Floryan's[9] theoretical results.

Figures 12-18 show both the experimental disturbance functions and the theoretical Görtler eigenfunctions for measurement locations of x/c = 0.175, 0.20, 0.225, 0.25, 0.275, 0.30, and 0.3375, respectively. These measurements cover the range from the beginning of the concave region at x/c = 0.175 to the end of the concave zone at x/c = 0.275 and into the convex zone beyond. These experimental disturbance functions were obtained from measurements taken as the laser control volume was scanned along the span at

nominally constant heights above the model surface. The mean velocity at each height was removed by use of a least squares linear fit of the data along the span. This technique not only removed the mean but also partially corrected for the general slope of the data caused by the small deflections of the floor supporting the laser optics. Then, the disturbance function for a given height was taken as the root mean square of the disturbance velocity over the measurement span. The theoretical Görtler eigenfunctions were obtained using Floryan's[9] code. For these calculations, the Blasius profile is assumed for the mean flow. The appropriate length scale is taken to be $\delta_D = \delta^*/1.7208$ where δ^* is the boundary-layer displacement thickness. This length scale is analogous to $\delta_r = \sqrt{\frac{\nu x}{U_\infty}}$ for the Blasius profile. The displacement thickness was computed using the Cebeci boundary-layer code with the theoretical pressure distribution and measured suction.[15] The experimental pressure distribution was not used because several of the pressure taps in the concave region were damaged. The nondimensional wave number is taken to be $\alpha\delta_D = 2\pi\delta_D/\lambda$ where λ is the experimentally determined wavelength $\lambda = 0.8$cm. The local Görtler number is defined as:

$$G = \frac{U_e \delta_D}{\nu}\sqrt{\frac{\delta_D}{r}}$$

where r is the local radius of curvature. Since the theoretical eigenfunctions are known only to within a multiplicative constant, they have been scaled to match the experimental maximum amplitude at each chord location. Table I gives the computed Görtler stability parameters for a wavelength of $\lambda = 0.8$ cm at $R_c = 1.0 \times 10^6$ and $M_\infty = 0.024$. Note that the nondimensional wave number $\alpha\delta_D$ grows as the boundary layer thickness increases in the compression portion of the concave region and decreases as the boundary layer thins in the expansion portion of the concave region. The local Görtler number reaches a maximum of around 10 near x/c = 0.2275. This corresponds to a maximum Görtler number of 29.9 based on the free stream velocity, the Blasius length scale δ_r and the local radius of curvature as given in reference 10. The theoretical growth rate can be seen to vary with the Görtler number up to a maximum of $\beta = 4.156$ at x/c = 0.2275.

The disturbance functions of figures 12-18 are plotted in nondimensional form with the abscissa being u_{rms}/U_e and the ordinate being $\eta = y/\delta_D$. As the boundary layer grows over the first half of the concave zone, the theoretical eigenfunctions move closer to the surface. Both the height of the maximum disturbance velocity and the point where the disturbance asymptotes to zero move closer to the wall. This trend is reversed as the boundary layer thickness decreases over the latter half of concave zone and the following convex region. Table II shows the variation of the maximum disturbance intensity with chord location. The disturbance intensity decreases slightly at the beginning of the concave zone and then increases to a peak at the downstream edge of the concave zone.

Only three experimental data points are available for comparison at the first two and last measurement stations. Better definition of the experimental disturbance function is possible over the central portion of the concave zone. At x/c = 0.175, the experimental points seem to indicate a disturbance layer which is thinner than its theoretical counterpart. For x/c = 0.225, 0.25, and 0.275, the theoretical and experimental eigenfunctions generally agree. If we neglect the anamolous point at $\eta = 1.4$, the experimental measurements at x/c = 0.225 lie very near to the theoretical curve. At x/c = 0.25, the height of maximum disturbance intensity is almost identical, but the experimental disturbance profile is fuller. The measured disturbance intensities above and below the height of maximum intensity slightly exceed the theoretical values. This difference may be due to the neglect of pressure gradient and suction effects in the theoretical model. The shape of the experimental disturbance profile at x/c = 0.275 agrees well with the theoretical prediction, but the experimental profile lies closer to the wing surface than does the theoretical curve. At x/c = 0.30, the experimental disturbance profile is very irregular. As noted earlier, there is an abrupt decrease in the measured disturbance intensity between x/c = 0.275 and 0.30. Perhaps not only the first Görtler mode but also other instability modes were amplified in the upstream concave region. Then in the convex region, the first Görtler mode may be damped more strongly than the other modes to produce the observed irregular profile.

The experimental and theoretical disturbance amplification data are shown in figure 19 as functions of chord locations. The experimental data are the $(u_{rms}/U_\infty)_{max}$ values from Table II. The theoretical curve was obtained by using the amplification ratio $e^{\int \beta dx}$ from Table I and matching the theoretical and experimental amplitudes at x/c = 0.175 where the concave zone begins. The experimental disturbance intensity decreases slightly at the beginning of the concave zone and then increases to a maximum at the end of the concave zone. In the convex zone beyond x/c = 0.275, the disturbance intensity decreases sharply. This result agrees with the flow visualization photographs which show an abrupt decrease in vortex streak contrast in the convex region (figure 3).[10] The theoretical curve increases steadily from the initial match point at x/c = 0.175 to a maximum value at the downstream end of the concave zone. No theoretical amplification values are available from the linear theory for the convex region; however, it is expected that the centrifugal effects will cause vortex damping there. Aside from the slight decrease in disturbance intensity at the beginning of the concave zone, the experimental disturbance amplification trend is in good agreement with the predictions of linear theory.

Thus, in summary, the trends of the experimental observations agree with the predictions of the Görtler linear stability theory. This agreement is observed in the disturbance wavelength, the eigenfunction shape, and the disturbance growth trends. Further experiments are planned to obtain more detailed disturbance velocity profiles at several chord and span locations.

Conclusions

1. Direct observation of the velocities, flow visualization, and statistical methods confirm constant Görtler vortex wavelength throughout the measurement region for fixed free-stream conditions.

2. The vortex wavelength was observed to vary with Görtler number in accordance with the maximum amplification line of linear stability theory as free-stream conditions were changed.

3. The eigenfunction shapes and growth trends agree with predictions from the Görtler linear stability theory.

Acknowledgment

This study was partially funded through NASA contract NAS1-18235.

References

1. Taylor, G. I.: Stability of Viscous Liquid Contained Between Two Rotating Cylinders. Phil. Trans. A223, pp. 289-343, 1923.

2. Görtler, H.: Instabilitat laminaren Grenzchichten an konkaven Wanden gegeniiber gewissen dreidimensionalen Storungen. ZAMM Vol. 21., No. 1, pp. 250-252, 1941.

3. Herbert, T.: On the Stability of the Boundary Layer Along a Concave Wall. Arch. Mechaniki Stosowanej, Vol. 28, No. 5-6, pp. 1039-1055, 1976.

4. Floryan, J. M.; and Saric, W. S.: Stability of Görtler Vortices in Boundary Layers. AIAA Journal, Vol. 20, No. 3, March 1983, pp. 316-324.

5. Ragab, S. A.; and Nayfeh, A. H.: Effect of Pressure Gradients on Görtler Instability. Paper No. 80-1377, AIAA 13th Fluid and Plasma Dynamics Conference, Snowmass, Colorado, July 14-16, 1980.

6. Hall, P.: The Linear Development of Görtler Vortices in Growing Boundary Layer. Journal of Fluid Mechanics, Vol. 30, pp. 41-58, 1961.

7. Tani, I.; and Aihara, Y.: Görtler Vortices and Boundary-Layer Transition. Z.A.M.P., Vol. 20, pp. 609-618, 1969.

8. Bippes, H.: Experimental Study of the Laminar-Turbulent Transition on a Concave Wall in a Parallel Flow. NASA TM-75243, 1978.

9. Floryan, J. M.: Stability of Boundary-Layer Flows Over Curved Walls. Ph. D. Thesis, Virginia Polytechnic Institute and State University, Blacksburg, Virginia, January 1980.

10. Mangalam, S. M.; Dagenhart, J. R.; Hepner, T. E.; and Meyers, J. F.: The Görtler Instability on an Airfoil. AIAA Paper No. 85-0491. Presented at the AIAA 23rd Aerospace Sciences Meeting, Reno, Nevada, January 14-17, 1985.

11. Dagenhart, J. R.; and Mangalam, S. M.: Disturbance Functions of the Görtler Instability on an Airfoil. Paper No. 86-1048, AIAA 4th Joint Fluid Mechanics, Plasma Dynamics and Lasers Conference, Atlanta, Georgia, May 12-14, 1986.

12. Stainback, P. C.; and Owen, F. K.: Dynamic Flow Quality Measurements in the Langley Low-Turbulence Pressure Tunnel. Paper No. 84-0621, AIAA 13th Aerodynamic Testing Conference, San Diego, California, March 1984.

13. Holmes, B. J.; Croom, C. C.; and Obara C. J.: Sublimating Chemical Method for Detecting Laminar Boundary-Layer Transition. NASA Tech. Brief LAR-13089, 1982.

14. Tani, I.; and Sakagami, J.: Boundary-Layer Instability at Subsonic Speeds. Proc. ICAS, Third Congress, Stockholm, pp. 391-403, 1962.

15. Kaups, K.; and Cebeci, T.: Compressible Laminar Boundary Layers with Suction on Swept and Tapered Wings. Journal of Aircraft, Vol. 14, No. 7, pp. 661-667, July 1977.

Table I

Computed Görtler stability parameters for a wavelength of λ = 0.8cm for $R_c = 1.0 \times 10^6$ and $M_\infty = 0.024$.

x/c	$\alpha\delta_D$	G	β	$e^{\int \beta dx}$
0.175	--	0	0	1.0
0.1825	0.3036	1.426	0.209	1.005
0.2025	0.3605	4.813	1.541	1.116
0.2275	0.4244	10.058	4.156	1.711
0.2525	0.3263	5.679	1.831	2.680
0.2675	0.2491	1.618	0.275	2.947
0.275	--	0	0	2.965

Table II

Experimental vortex intensities for $R_c = 1.0 \times 10^6$ and $M_\infty = 0.024$.

x/c	$(u_{rms}/U_e)_{max}$	$(u_{rms}/U_\infty)_{max}$
0.175	0.022	0.017
0.20	0.021	0.014
0.225	0.030	0.022
0.25	0.032	0.031
0.275	0.047	0.050
0.30	0.024	0.030
0.3375	0.020	0.027

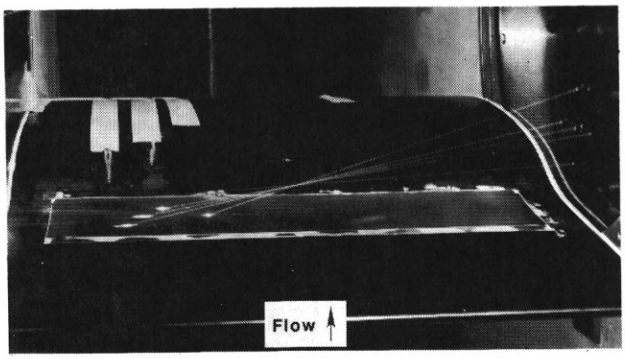

Figure 1. Görtler model in LTPT.

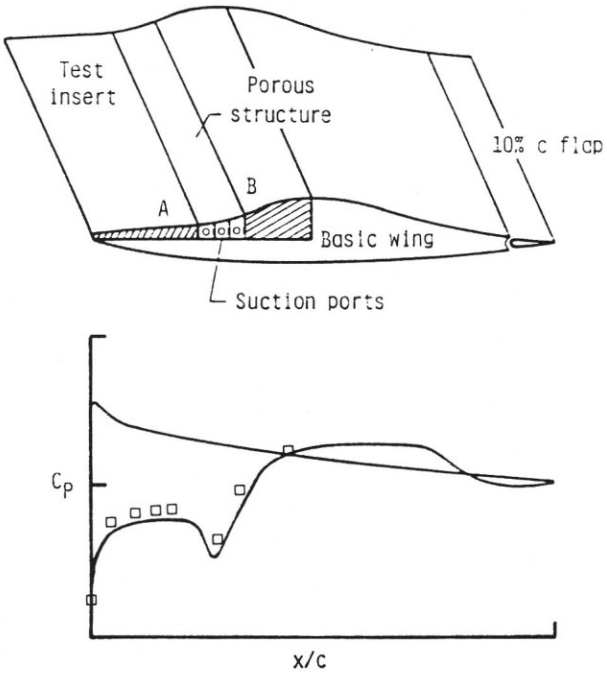

Figure 2. Model schematic diagram and pressure distribution.

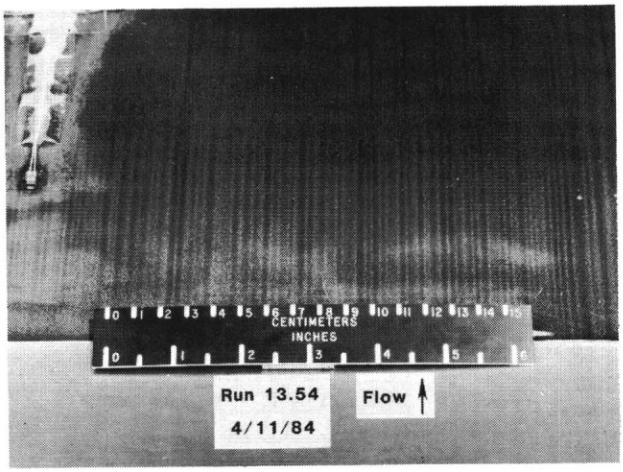

Figure 3a. Flow visualization using sublimating chemicals $M_\infty = 0.05$, $R_c = 2.24 \times 10^6$.

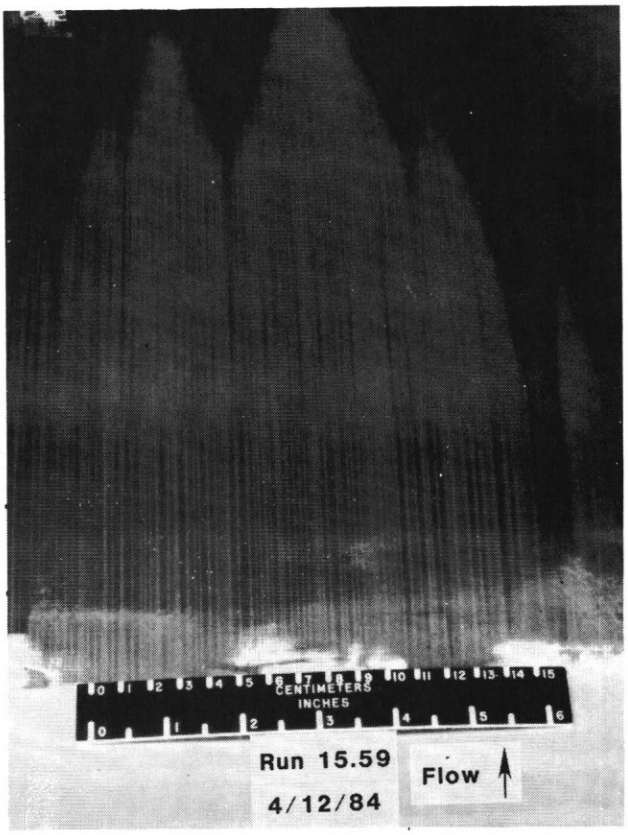

Figure 3b. Flow visualization using sublimating chemicals $M_\infty = 0.075$, $R_c = 3.21 \times 10^6$.

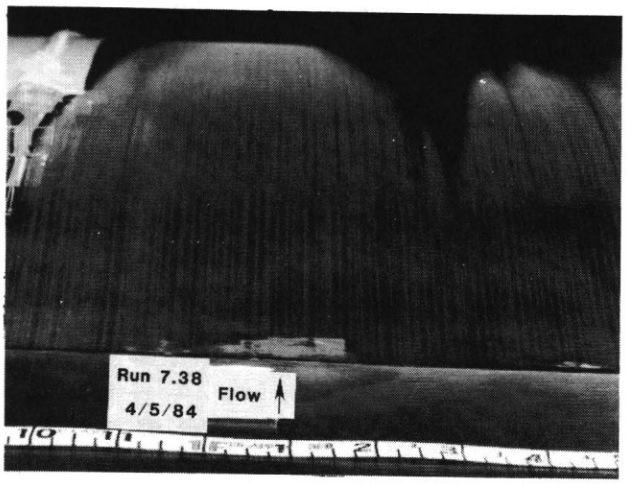

Figure 3c. Flow visualization using sublimating chemicals $M_\infty = 0.089$, $R_c = 3.67 \times 10^6$.

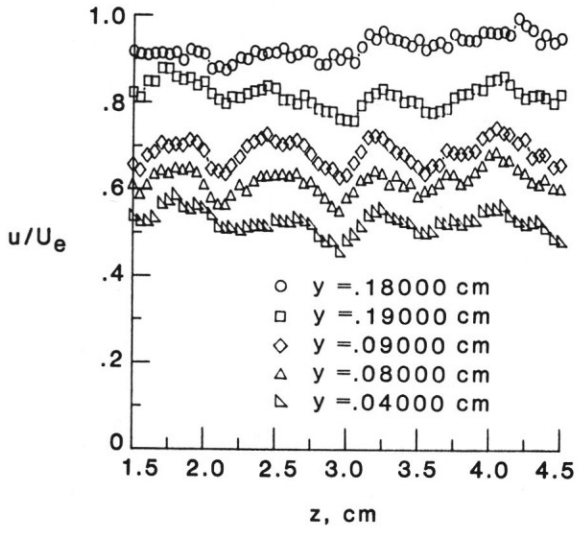

Figure 4. Spanwise variation of streamwise velocity component $R_c = 1.0 \times 10^6$, G = 5.679, x/c = 0.25.

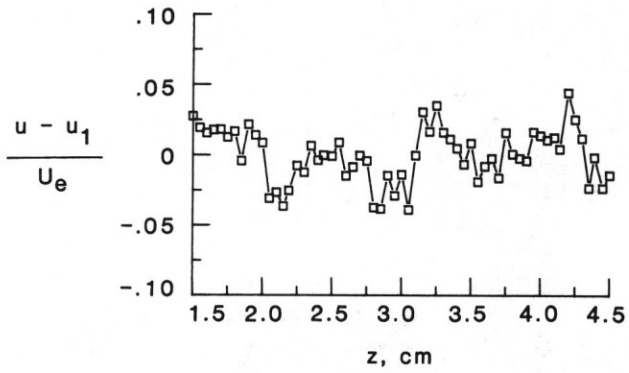

a) Velocity fluctuations

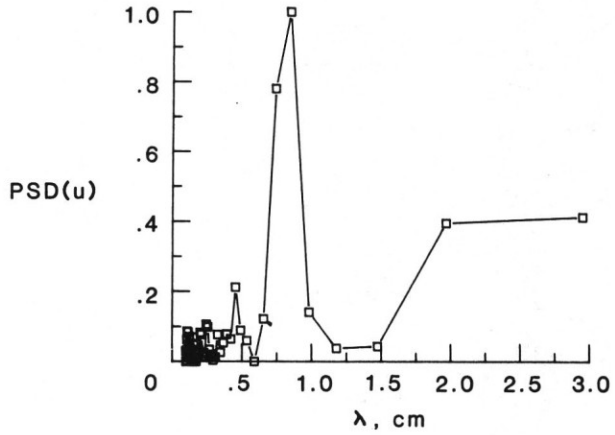

b) Power spectral density

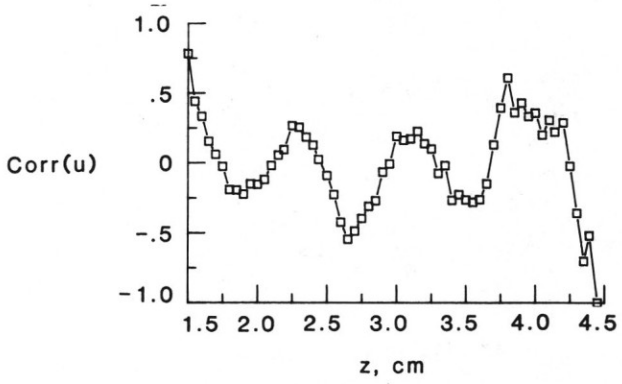

c) Correlation function

Figure 5. Streamwise velocity fluctuations, power spectral density, and correlation function at x/c = 0.25 and y = 0.18cm.

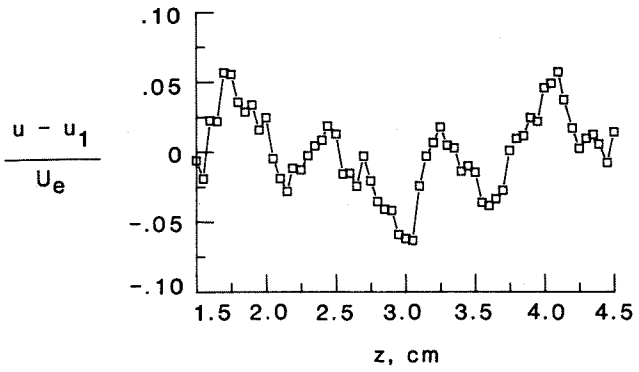

a) Velocity fluctuations

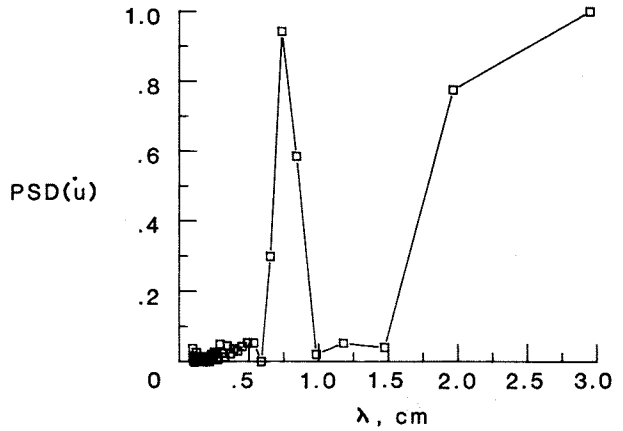

b) Power spectral density

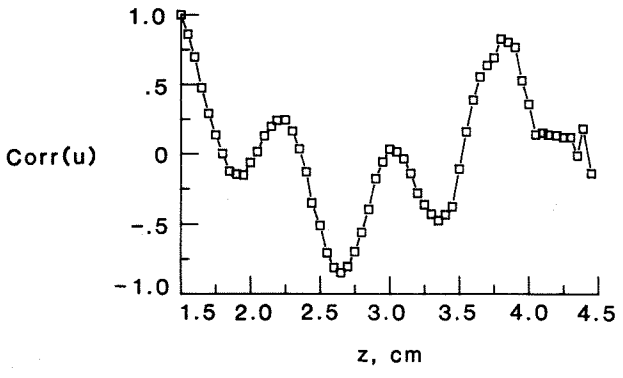

c) Correlation function

Figure 6. Streamwise velocity fluctuations, power spectral density, and correlation function at x/c = 0.25 and y = 0.13cm.

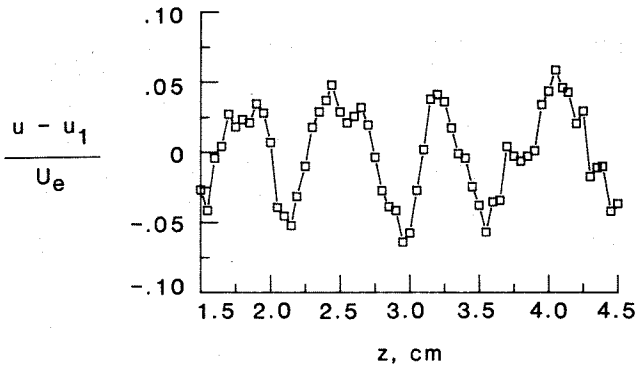

a) Velocity fluctuations

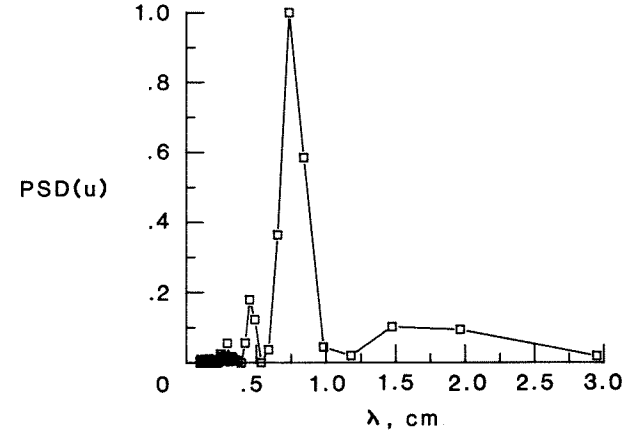

b) Power spectral density

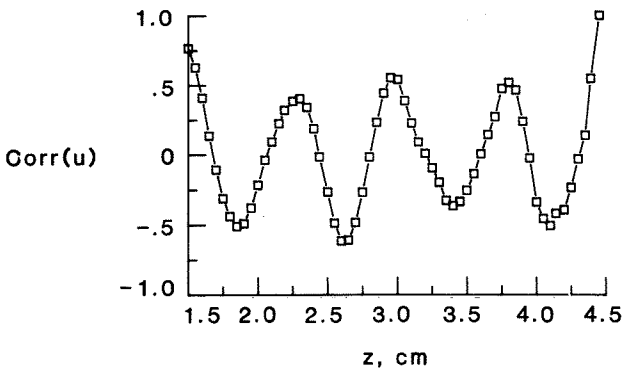

c) Correlation function

Figure 7. Streamwise velocity fluctuations, power spectral density, and correlation function at x/c = 0.25 and y = 0.09cm.

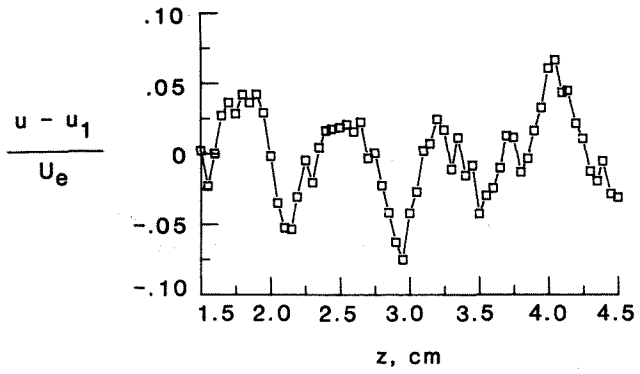

a) Velocity fluctuations

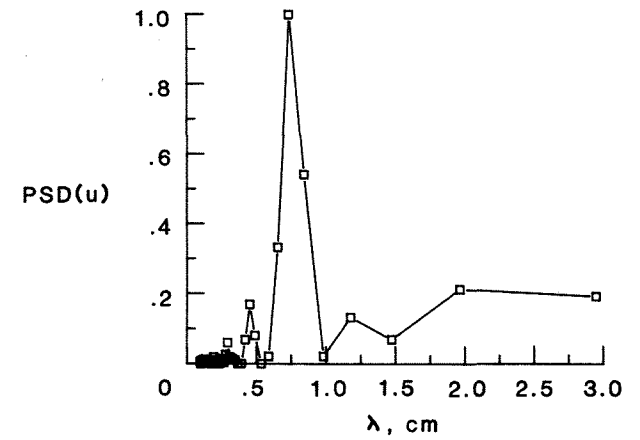

b) Power spectral density

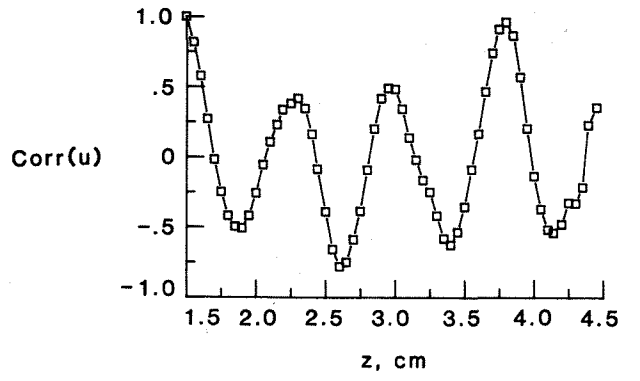

c) Correlation function

Figure 8. Streamwise velocity fluctuations, power spectral density, and correlation function at x/c = 0.25 and y = 0.06cm.

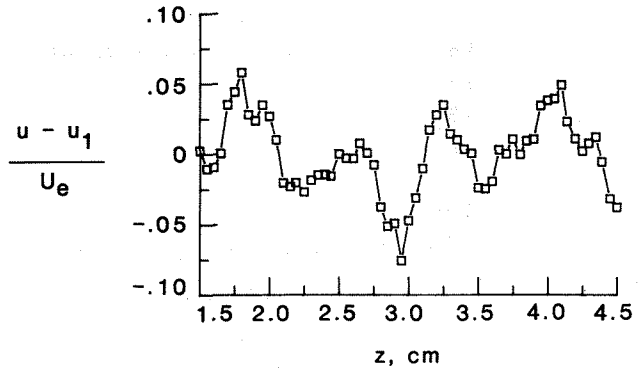

a) Velocity fluctuations

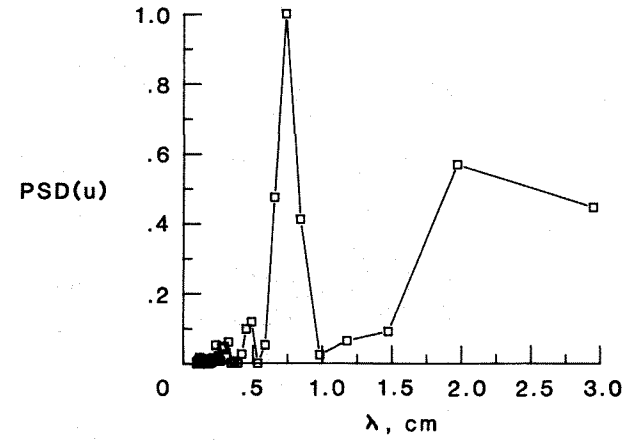

b) Power spectral density

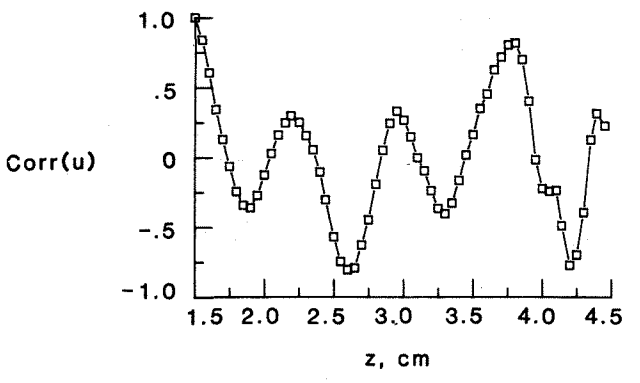

c) Correlation function

Figure 9. Streamwise velocity fluctuations, power spectral density, and correlation function at x/c = 0.25 and y = 0.04cm.

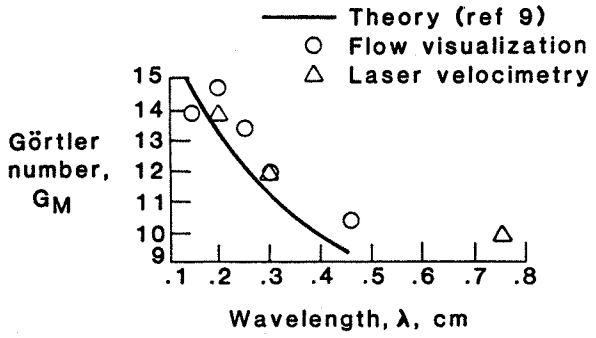

Figure 10. Variation of dimensional wavelength with Görtler number, comparison with theory.

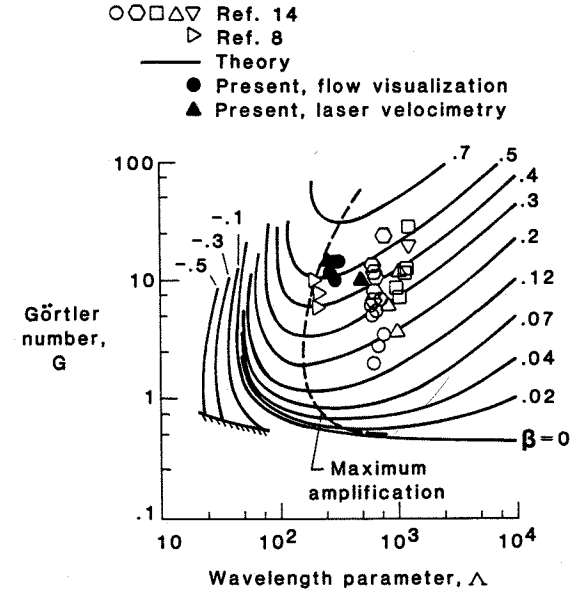

Figure 11. Variation of nondimensional wavelength parameter with Görtler number, comparison with theory and other experiments.

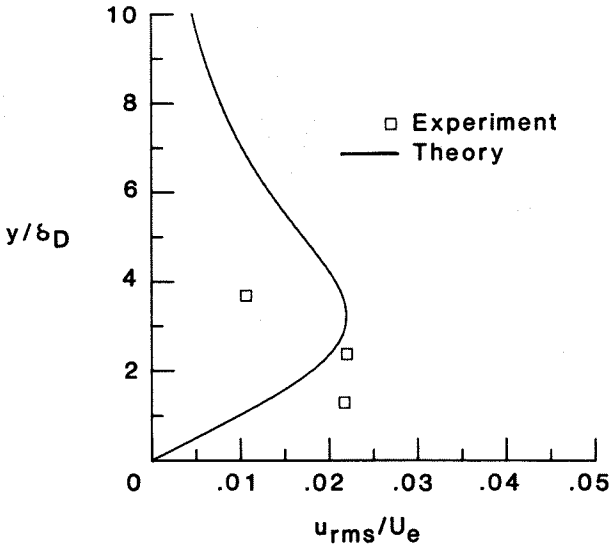

Figure 12. Streamwise velocity disturbance function at x/c = 0.175, G = 1.426.

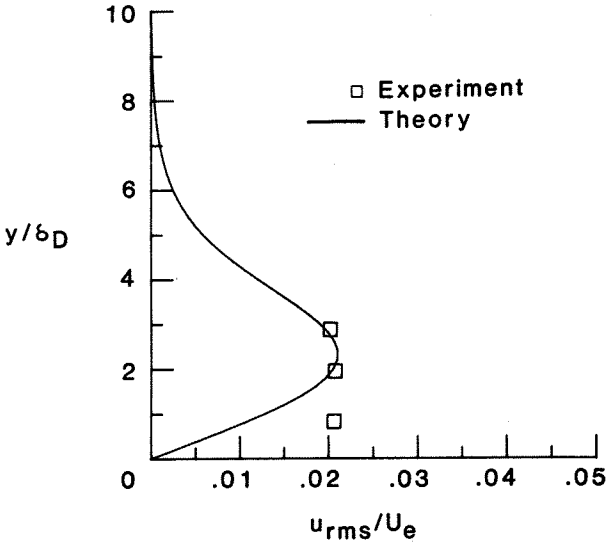

Figure 13. Streamwise velocity disturbance function at x/c = 0.20, G = 4.813.

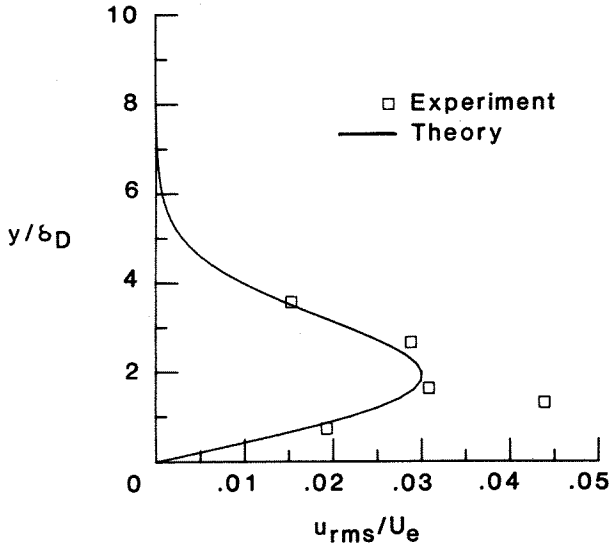

Figure 14. Streamwise velocity disturbance function at x/c = 0.225, G = 10.058

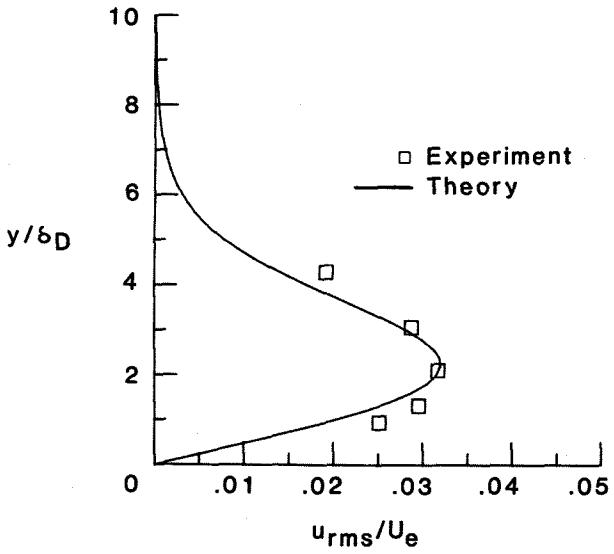

Figure 15. Streamwise velocity disturbance function at x/c = 0.25, G = 5.679.

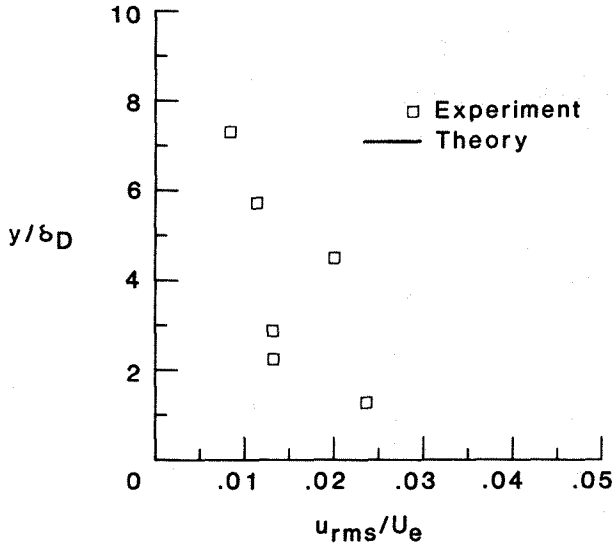

Figure 17. Streamwise velocity disturbance function at x/c = 0.30.

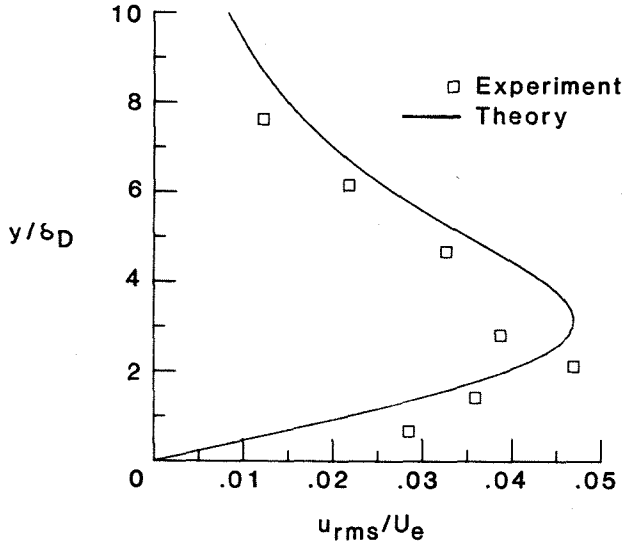

Figure 16. Streamwise velocity disturbance function at x/c = 0.275, G = 1.618.

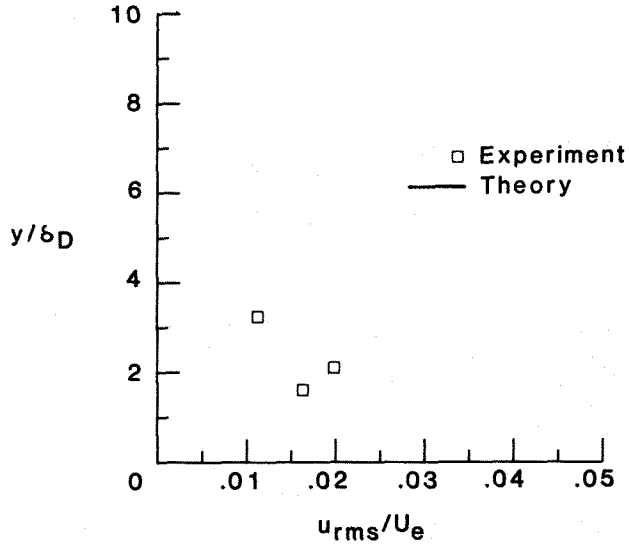

Figure 18. Streamwise velocity disturbance function at x/c = 0.3375.

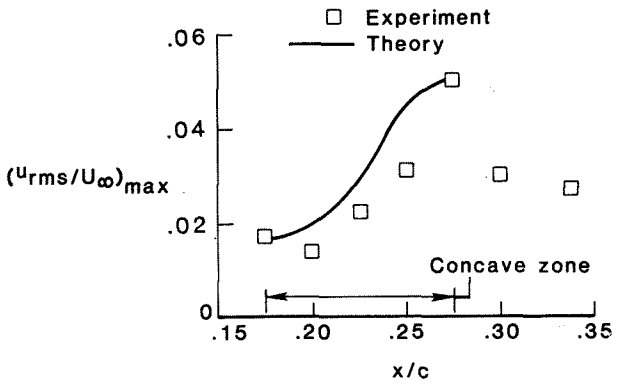

Figure 19. The variation of the maximum disturbance amplitude over the measurement range.